Synthetic Metals 211 (2016) 1–13

Contents lists available at ScienceDirect

Synthetic Metals

journal homepage: www.elsevier.com/locate/synmet

Synthesis, structural analysis, spectrophotometric measurements and semiconducting properties of 3-phenyl azo-4-hydroxycoumarin thin films

M.M. Makhlouf[a,b,c,*], H.M. Zeyada[b]

[a] Department of Physics, Faculty of Applied Medical Sciences at Turabah, Taif University, 21995, Saudi Arabia
[b] Department of Physics, Faculty of Science, Damietta University, 34517 Damietta, Egypt
[c] Department of Physics, Damietta Cancer Institute, Damietta, Egypt

ARTICLE INFO

Article history:
Received 23 August 2015
Received in revised form 18 October 2015
Accepted 20 October 2015
Available online xxx

Keywords:
Coumarins
Thin films
Structural properties
Optical constants
Electrical conductivity

ABSTRACT

3-phenyl azo-4-hydroxycoumarin, PAHC, compound was synthesized by reacting aniline diazonium salt with 4-hydroxy coumarin. The thin films of PAHC were prepared on the glass and quartz substrates by thermal evaporation technique under vacuum pressure 10^{-5} mbar. The structure of thin films was characterized using X-ray diffraction, XRD, and Fourier transformation infrared, FTIR, techniques. The XRD pattern for the pristine PAHC thin film showed nanocrystallites distributed in amorphous matrix. Annealing at 423 K improved the crystallinity of films and the crystallite size is in the range 23–36 nm. FTIR showed different vibrational modes, observed in infrared spectra of the powder, pristine and annealed thin films, were assigned to the molecular bonding structure of PAHC compound. The optical properties of PAHC thin films were investigated by the spectrophotometer measurements of the pristine and annealed PAHC films in the range 200–2100 nm. The refractive and absorption indices of the pristine and annealed PAHC films were calculated from measured transmittance and reflectance data. The results showed that the refractive and absorption indices of thin films are influenced with increasing annealing temperature. The direct allowed transitions were the most probable transition and the optical band gap was found to vary from 2.14 to 2.21 eV with increasing annealing temperature. The single oscillator model was applied in the normal region of dispersion spectrum to determine the dispersion parameters and it is noted that they are decreased with annealing temperature. The AC electrical conductivity, σ_{AC}, and the real and imaginary parts of dielectric constants measurements were investigated in temperature range 304–413 K and frequency range 0.1–100 kHz; they confirmed semiconductor behavior of the PAHC films.

1. Introduction

Organic semiconductors are very interesting area of current scientific research. There are many significant developments made in the synthesis, characterization and application oriented development of these materials. The electrical and optical properties of organic semiconductors are mainly responsible for the growing interest as an attractive area of research. The interest in the thin films of semiconductors is high as they show good luminescence, fluorescence and absorption properties at the nano-scale whereas there is no emission from them in their bulk form [1]. Further studies on organic semiconductors are very interesting because of their size dependent optical properties which can lead to many technologically important applications such as organic light emitting diode [2], integrated flash memory [3] and solar cell [4] devices. In the fastest growing field of the nanoscience and nanotechnology, the integration of optoelectronic devices with the nano- and micro-electronics which show efficient optical properties along with their integration in electronic technology is needed. Organic semiconductors are considered to be ideal candidates for optoelectronic applications of optical lighting and display applications because they show emission or absorption in the visible region [5].

Coumarins are a family of organic semiconductors which are manufactured from natural resources and others they were synthesized from molecular structure (1,2-benzopiron) [6]. Coumarins and their derivatives show absorption and fluorescence characteristics which could be enhanced by attaching of appropriate functional groups at suitable positions in the structure of coumarin which causes a change in mobility of electrons [7,8]. The

* Corresponding author at: Department of Physics,Faculty of Applied Medical Sciences at Turabah, Taif University, 21995, Saudi Arabia. Tel.: +966 533776359; fax: +20 572403868.
E-mail addresses: m_makhlof@hotmail.com, m.m.makhlouf@hotmail.com (M.M. Makhlouf).

http://dx.doi.org/10.1016/j.synthmet.2015.10.019
0379-6779/

electron donor groups such as amino, hydroxyl situated at the position-7 in coumarin and heterocyclic electron acceptors such as benzothiazole and at the position-3 of benzoxazole should induce bathochromicity and shows strong fluorescence [7–9]. Coumarins were also employed as photo-controlled molecules opening and closing a silica pore, where from guest molecules are released, or in photodegradable polymers [10,11]. Coumarin dimers play an important role as photocleavable linker molecules for two-photon absorption controlled drug delivery [12]. The refractive index changes accompanying the photocleavage of the cyclobutane structure which may be used in optical and holographic recording [13].

Hydroxycoumarins and their derivatives possess many remarkable properties; they are well known for their high sensitivity as excellent lasing properties in the blue–green region [14] and application as luminescent colorants for bio-substrates, fluorescent whiteners for polyster and polymide fabrics [15] and photoprotective compound used as a sunscreen component [16]. The electronic structure of hydroxycoumarins, including their UV light absorption ability, has become the subject of much interest. Absorption spectra of hydroxycoumarins and their derivatives have been studied [17,18]. Three main absorption bands of coumarins have assigned to $\pi \rightarrow \pi^*$ transitions in the long wavelength region. The first absorption band of hydroxycoumarins belongs to transition from HOMO → LUMO which is localized on the carbon atoms of the phenyl ring and the lactone ethylene bond. The second transition band is due to (HOMO − 1) → LUMO transition and the third band belongs to the transition HOMO → (LUMO + 1) [17,18]. The intensity, shape and position of these bands depends on the type of solvent, for example the maximum positions of electronic absorption for coumarins derivatives in ethanol are very close to those in cyclohexane [18]. 4-Hydroxycoumarin derivatives were studied by spectral methods: electronic absorption spectroscopy [19], IR spectroscopy [20] and X-ray crystal analysis [21]. The knowledge of absorption and fluorescence characteristics of these compounds with different substituents under varying condition of solvents [22], temperatures [23] and pH [24] are important for understanding the operation of tunable dye lasers at maximum efficiency. The electronic absorption and emission spectra as well as fluorescence quantum yield of 3-(benzothiazol-2-yl)-7-hydroxycoumarin (BTHC) were measured in different solvents and are affected by solvent polarity. BTHC acts as good laser dye upon pumping with nitrogen laser (λ_{max} = 337 nm) in ethanol and gives laser emission with maxima at 508 and 522 nm [25]. Effect of solvents of varying polarities on absorption and fluorescence spectra and dipole moment of laser dye: 7-diethylamino-3-thenoylcoumarin has been investigated. A bathochromic shift observed in absorption and emission spectra with increasing solvent polarity, which implied that the involved transition is $\pi \rightarrow \pi^*$ [26]. Although, several reports have been emerged on the physical properties of coumarins [17–26], the optical and electrical transport properties of many 4-hydroxycoumarin derivatives have not yet been systematically studied, in our research efforts focus on the study of structural formation, optical constants, dispersion parameters and semiconducting behavior of 3-phenyl azo-4-hydroxycoumarin, PAHC, thin films and influence of the annealing temperature on their structural, optical and electrical properties.

2. Experimental details

2.1. Synthesis of 3-phenyl azo-4-hydroxycoumarin

The chemicals used in the present work were obtained from Sigma–Aldrich Co. and used as received without any further purification or treatment. The synthetic procedure route

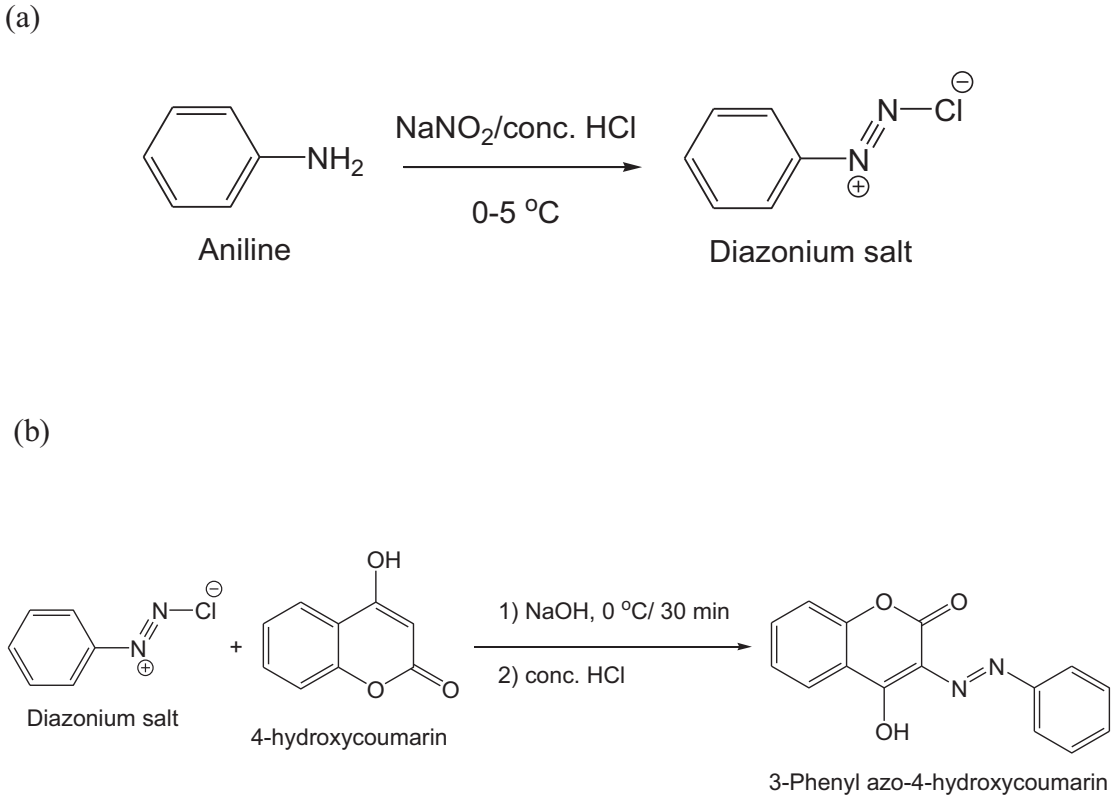

Scheme 1. Mechanism of synthesis of 3-phenyl azo-4-hydroxycoumarin, PAHC: (a) formation of diazonium salt and (b) coupling reaction of diazonium salt with 4-hydroxycoumarin.

for obtaining azo-coumarin derivative compound, 3-phenyl azo-4-hydroxycoumarin, which is used in the present work is shown in Scheme 1.

(1) Aniline (1 mmol) was mixed 2.5 mL of conc. HCl (36%) and 2.5 mL of an aqueous solution of sodium nitrite ($NaNO_2$, 4 N) at 0 °C in ice bath. The reaction mixture was kept under stirring at 0–5 °C till the corresponding diazonium salt is formed (~2 h), as shown in Scheme 1(a). The reaction mixture was kept under vacuum for slow evaporation of the solvent till the solid diazonium salt is precipitated and then filtrated out and washed with diethyl ether and dried in oven.

(2) An aqueous solution of aniline diazonium salt which formed in the previous step (1 mmol) was added dropwise to an alkaline solution of 4-hydroxycoumarin (1 mmol) (NaOH, 1 N, 5 mL) at 0 °C. The reaction mixture was kept under stirring at 0 °C for 30 min till the temperature being 5–10 °C. The reaction mixture was

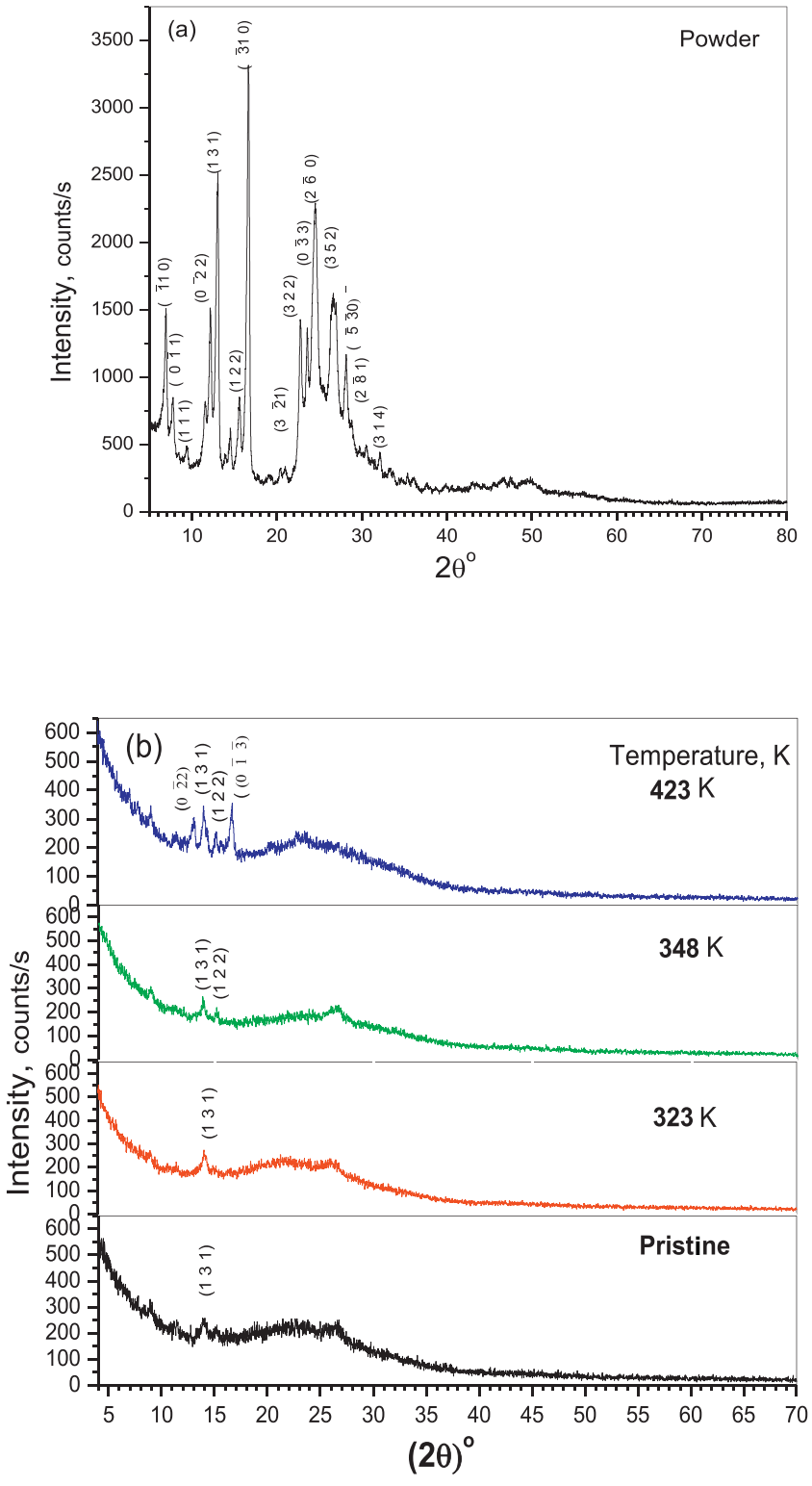

Fig. 1. X-ray diffraction patterns of PAHC: (a) powder, (b) pristine and annealed films at 323 K, 348 K and 423 K for 1 h.

Table 1
Variation of crystallite size (D), microstrain (M), average inter-separation distance (R) and dislocation density, δ, for the pristine and annealed thin films.

Thin film condition	Pristine	Annealed at 348 K		Annealed at 423 K			
2θ	14.1°	14.1°	15.9°	12.8°	14.1°	15.9°	16.6°
D (nm)	22.7	23.2	18.6	23.4	29.3	33.7	36.1
$M \times 10^{-3}$	1.61	1.58	1.97	1.56	1.25	1.10	1.01
R (Å)	3.96	3.96	3.70	4.35	3.96	3.52	3.37
$\delta \times 10^{-3}$ (nm)$^{-2}$	1.94	1.86	2.89	1.83	1.17	0.88	0.76

neutralized by conc. HCl (HCl was added dropwise till pH of the reaction media be ~7). A yellow colored solid precipitate was obtained in the reaction media was filtered off, washed many times with distilled water and dried in oven. The final product of 3-phenyl azo-4-hydroxycoumarin, PAHC, was recrystallized in ethanol (50%). The purity of compound was checked by TLC. The overall synthetic scheme is shown in Scheme 1.

2.2. Preparation of PAHC thin films and physical measurements

Thin films of PAHC were prepared by thermal evaporation technique using a high vacuum coating unit (Edwards E306 A, England). During the deposition process, the vacuum pressure is about 10^{-5} mbar. The films were deposited onto clean glass and optical flat quartz substrates for structural, electrical and optical measurements, respectively. These substrates were carefully cleaned by chromic acid for 15 min and then rinsed by deionized water. Evaporation of the powder of PAHC material is carried out with quartz crucible heated by boat-shaped molybdenum heater. The deposition rate and the film thicknesses were measured during the evaporation using a quartz crystal thickness monitor (Model TM-350 MAXTEK, Inc., USA) attached to the coating system. The grown film thickness of PAHC is 140 nm with deposition rate 2.5 Å/s. A shutter, fixed near to the substrate was used to avoid any probable contamination on the substrates in the initial stage of evaporation process and to control the thickness of films accurately.

The X-ray diffraction measurements are carried out by using Philips X-ray diffraction system (model X'Pert Pro) with utilized monochromatic CuKα radiation of λ = 1.5418 Å. The applied voltage and tube current are 40 kV and 30 mA, respectively. The range of scanning diffraction angle, 2θ, was from 5 to 75° with step time 1 s and step size of $2\theta = 0.1°$. Fourier transform infrared (FTIR) spectra are recorded using PerkinElmer 1340 spectrophotometer in spectral wave number range from 4000 to 400 cm^{-1}.

Optical measurements are good methods for estimating many properties of semiconductors. The transmittance, $T(\lambda)$, and reflectance, $R(\lambda)$, spectra of the films were measured at normal incidence of light in the spectral range 200–2200 nm using a double-beam spectrophotometer (JASCO model V-570

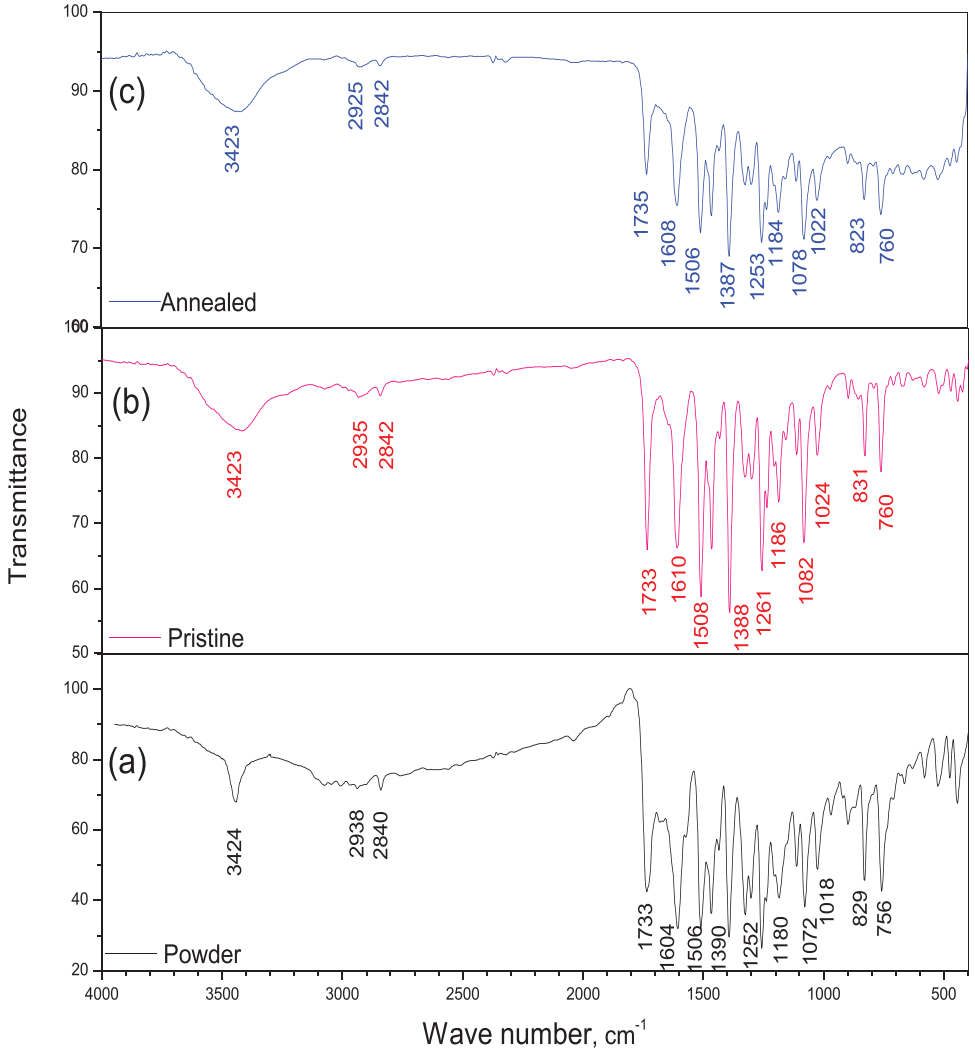

Fig. 2. FTIR for PAHC: (a) powder, (b) pristine film and (c) annealed film (423 K for 1 h).

Table 2
FT-IR of PAHC: powder, pristine film and annealed film at 423 K.

Wavenumber (cm^{-1})			Vibrational assignments
Powder	Pristine film	Annealed film at 423 K	
3425	3423	3423	ν (O—H)
2939	2935	2926	ν (C—H)
2840	2842	2839	ν (C—H)
1733	1733	1735	ν (C=O)
1604	1610	1608	ν (N≡N) asymmetry
1506	1508	1506	ν (C=C) in phenyl ring
1466	1466	1468	ν (C=C) in phenyl ring
1390	1389	1387	δ (C—H)
1252	1261	1253	δ (N—H), ν (*N*-phenyl ring), δ (C—N), ν (C—C)
1186	1186	1184	δ (N—H), ν (*N*-phenyl ring), δ (C—N), υ (C—C)
1149	1147	1145	ν (C—O) asymmetry
1115	1115	1113	δ (C—H) vibration
964	973	972	ν (C—C), ν (C—N), ν (C—O)
897	899	900	γ (C—H)
829	831	824	γ (C—H)
756	759	759	γ (C—H)
665	673	673	γ (C—H)
634	629	632	δ (C—C), δ (C—N), δ (C—O) in phenyl ring
577	582	582	δ (C—C), δ (C—N), δ (C—O) in phenyl ring
544	538	539	δ (C—C), δ (C—N), δ (C—O) in phenyl ring
425	428	422	In plane deformation of phenyl ring

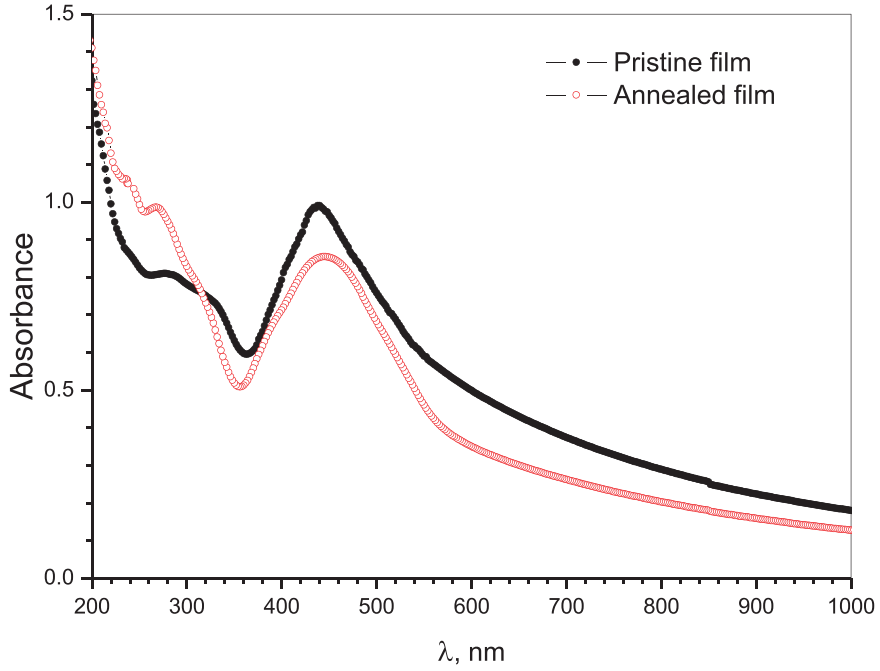

Fig. 3. Spectral distribution of the absorbance for the pristine and annealed (423K for 1 h) PAHC thin film.

UV–vis–NIR) for deposited films. An uncertainty of 2% was given by the manufacturer for the measurements obtained by this spectrophotometer. This spectrophotometer compares the signal coming out from the sample to that one of a reference beam. Additionally, a base line was adjusted prior to the actual measurements to calibrate the instrument. These measurements were also performed for the films after being annealed at 423 K with a soaking time of 1 h.

Sample of sandwich structure Au/PAHC/Au is used for electrical measurements. The thickness of PAHC is 140 nm. Au electrodes were carried out using basket-shaped of tungsten filament by thermally evaporated technique. The *I–V* measurements of sandwich structure showed that Au electrodes act as Ohmic contact. The active area of the device is 7.5 mm^2. The AC measurements were carried out using a programmable automatic LCR bridge (Stanford model SR 720 LCR Meter). The measurements were performed in frequency range 0.1–100 kHz and temperature range 304–423 K. The temperature was recorded using NiCr–NiAl thermocouple. All measurements were taken under dark inside tubular furnace.

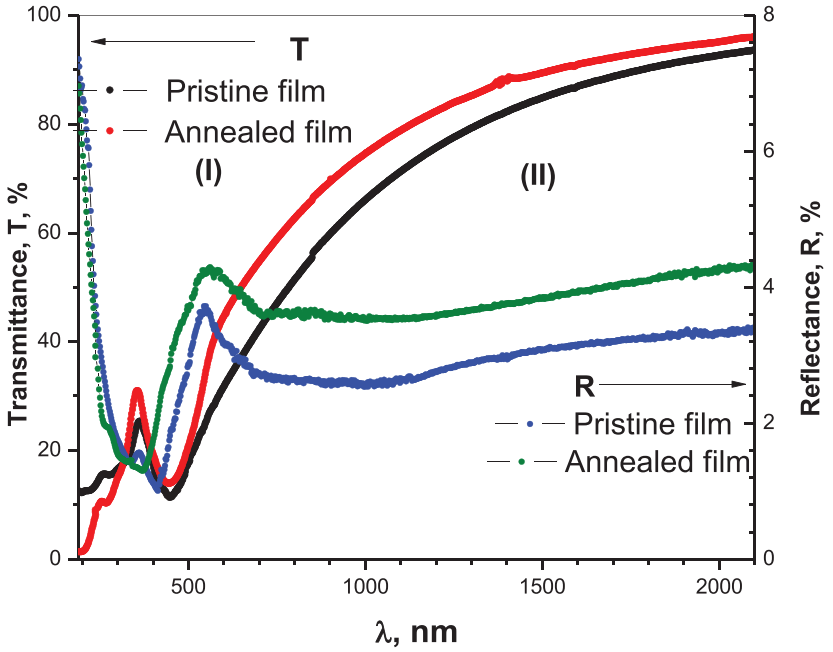

Fig. 4. Spectral distribution of the transmittance, *T*, and reflectance, *R*, for the pristine and annealed PAHC thin films.

3. Results and discussion

3.1. Structural properties

3.1.1. X-ray diffraction patterns

The XRD pattern for PAHC in powder form is shown in Fig. 1(a). It is observed that the powder of PAHC exhibits many peaks with different intensities . The diffraction peaks in powder spectra are indexed and the lattice parameters are determined with the aid of CRYSFIRE computer program [27]. The values of Miller indices, *h k l*, for each diffraction peak are calculated using CHEKCELL computer program [28]. The results show that PAHC powder has a triclinic crystal system with space group P1 and the lattice parameters are estimated as: $a = 16.217$ Å, $b = 28.948$ Å, $c = 14.879$ Å, $\alpha = 101.98°$, $\beta = 99.71°$ and $\gamma = 75.82°$. The indicated Miller indices (*h k l*) on each diffraction peak have been calculated by using CRYSFIRE system for automatic powder indexing and LMPG-Suite programs for the interpretation of X-ray experiments [27,28]. The XRD pattern for PAHC thin films with thickness of 140 nm is shown in Fig. 1(b). The broad halo in the diffraction pattern is due to

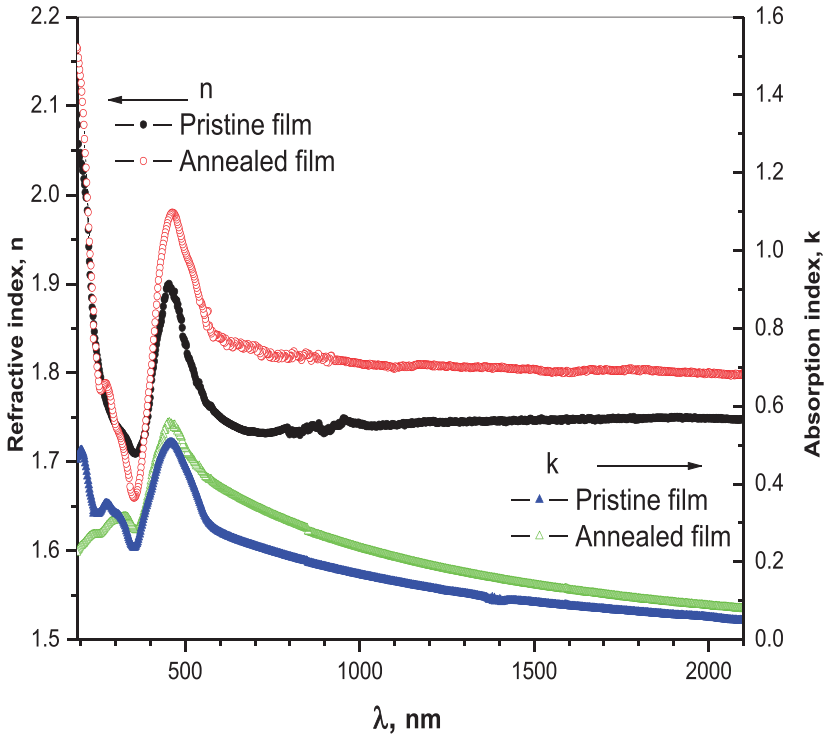

Fig. 5. The spectral behavior of the refractive index, *n*, and absorption index, *k*, for the pristine and annealed PAHC thin films.

amorphous PAHC phase and a single peak as observed around ($2\theta = 14.1^\circ$) indicates that the nanocrystallite are preferably oriented with (131) plane parallel to the surface of substrate. Annealing temperatures up to 423 K increases the intensity of the peak at ($2\theta = 14.1^\circ$) and also creates a new diffraction peaks at ($2\theta = 12.8^\circ$, 14.1°, 15.9°, 16.6°) corresponding to diffraction from $(0\bar{2}2)$,(122) and $(\bar{3}\bar{1}0)$ planes, respectively. The increase in the number and integrated intensity of diffraction planes with increasing annealing temperature indicates improvement in the crystallinity of PAHC films.

From XRD Pattern data, the structural parameters can be estimated which includes: the crystallite size, D, and the dislocation density, δ.

The mean crystallite size, D, was estimated by using the Debye-Scherrer formula as [29]:

$$D = \frac{K_S \lambda}{\beta \cos\theta} \quad (1)$$

where λ is the X-ray wavelength of CuKα (0.15418 nm), θ is the corresponding Bragg diffraction angle and K_S is the Scherrer's constant, which is of the order of unity ($\approx$0.95) [30]. Also β; the half width at maximum intensity of diffraction peak is given by the relation:

$$\beta = \sqrt{\beta_f^2 - \beta_p^2} \quad (2)$$

where β_f is the width of the strong peak at half maximum intensity for the thin film and β_p is the width of the strong peak at half maximum intensity for the powder. It is observed that the crystallite size increases with increasing annealing temperature of the films. The microstrain, M, of the pristine and annealed PAHC thin films were evaluated from the equation [30].

$$M = \frac{\beta}{4\tan\theta} \quad (3)$$

The microstrain decreases with the increase of annealing temperature, that decreasing in microstrain may be due to the decrease in lattice defects among the grain boundary, which is attributed to the decrease of breadth of diffraction peak with increasing the annealing temperature of the films. The average inter-separation distance, R, in the amorphous region of pristine and annealed PAHC thin films were evaluated from the position of the half maximum intensity [29,30].

$$R = \frac{5\lambda}{8\sin\theta} \quad (4)$$

The dislocation density, δ, is defined as the number of dislocation lines per unit area of the crystal; it was evaluated from the formula [29,31]

$$\delta = \frac{1}{D^2} \quad (5)$$

The values of crystallite size, microstrain and dislocation density for pristine and annealed PAHC thin films are listed in Table 1. It was observed that the crystallite size increases and the dislocation density and microstrain decrease with increasing the annealing process.

3.1.2. FTIR spectroscopy

Fig. 2 illustrates the FTIR spectra for the powder, pristine and annealed thin films of PAHC. According to Table 2; in the high vibration frequencies, the strong and broad band of PAHC is at $3424 \pm 1\ cm^{-1}$ which gives the stretching mode of hydroxyl of coordinated water molecules [32]. In the region between 3000 and 2800 cm^{-1}, the bands are associated with anti-symmetric C—H stretching vibration in alkyl functional group. The characteristic bands, fingers print, of PAHC can be noted at the spectrum below 1750 cm^{-1} and most of these bands appear narrower and stronger than in high frequency region. Several characteristics of these bands also were related to the different functional groups. The peak at $1733 \pm 2\ cm^{-1}$ was assigned to C=O stretching frequency ($\nu_{c=o}$) while that at 1507 ± 1 and $1466 \pm 2\ cm^{-1}$ corresponds to aromatic C=C stretching ($\nu_{c=c}$). The sharp and strong band at $1607 \pm 3\ cm^{-1}$ refers to the characteristics vibration band of azo functional group which is associated with the anti-symmetric stretching vibration. The different mode of vibrations of N—H bending, N-ring stretch and C—N bending are identified by the presence of characteristics bands in the region between 1388 ± 2, 1255 ± 6 and $1182 \pm 2\ cm^{-1}$ [33]. The bands in the region between 900 and 650 cm^{-1} are related to C—H out of plane bending vibrations. The bands are located at region less than 650 cm^{-1} are attributed to in plane deformation of phenyl ring.

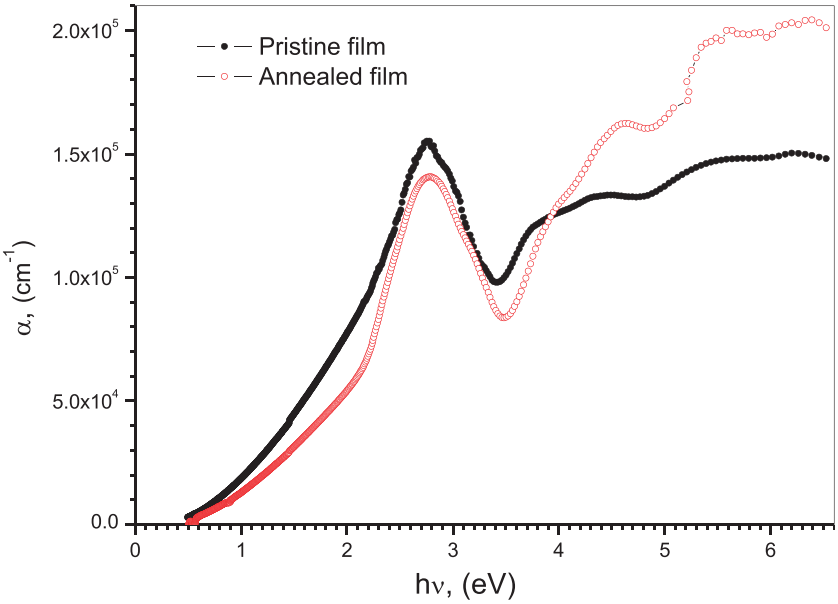

Fig. 6. Absorption coefficient, α, dependence on photon energy, $h\upsilon$, for the pristine and annealed PAHC thin films.

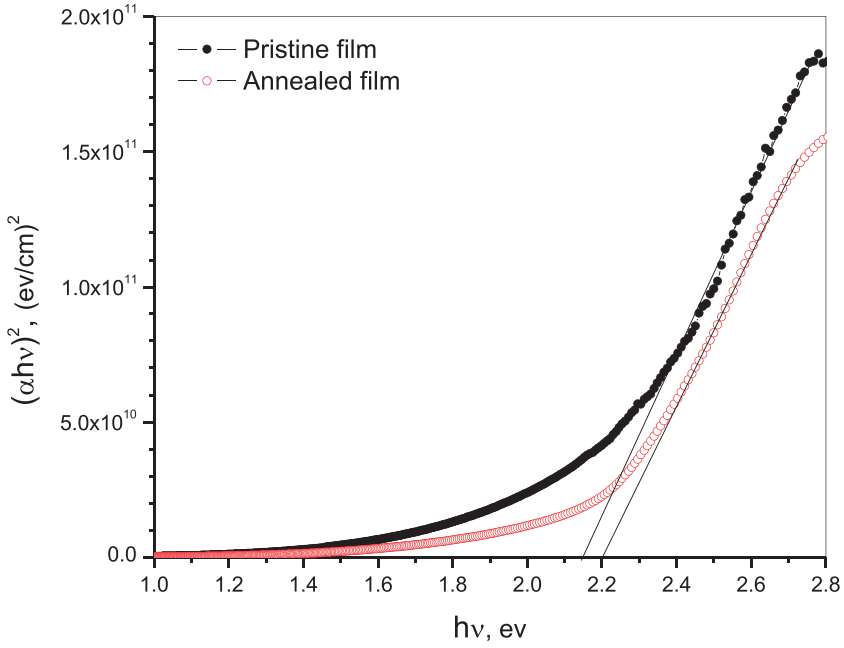

Fig. 7. The relation between $(\alpha h\nu)^2$ and photon energy, $h\upsilon$, for the pristine PAHC thin films and after annealing at 423 K for 1 h.

3.2. Optical properties

The absorption spectrum gives useful information about the features concerning the band structure of materials. Fig. 3 shows the absorption spectrum, A, for PAHC thin film as a function of wavelength, λ, in the UV–vis. spectral region. The absorption spectra exhibit two peaks that can be attributed to the orbital molecular transition from bonding to antibonding molecular orbital [34]. The electronic absorption of PAHC depends on hydroxyl and azo functional groups. Absorption spectrum of PAHC thin film contains azo band which has absorption peak at 447 nm located in the visible region of spectra and it is ascribed to the absorption band of the $n \rightarrow \pi^*$ transition. The phenyl ring and the hydroxyl groups have absorption peak at 271 and 240 nm, respectively, in UV region of spectra and are ascribed to the absorption of the $\pi \rightarrow \pi^*$ transition.

Table 3
The optical energy gap (E_g) and dispersion parameters of pristine and annealed PAHC thin films.

Thin film	E_g (eV)	E_o (eV)	E_d (eV)	ε_∞	ε_L	N/m^* (kg^{-1} m^{-3})
Pristine	2.14	5.18	10.58	3.04	3.06	1.59×10^{55}
Annealed	2.21	4.75	9.98	3.22	3.27	1.11×10^{55}

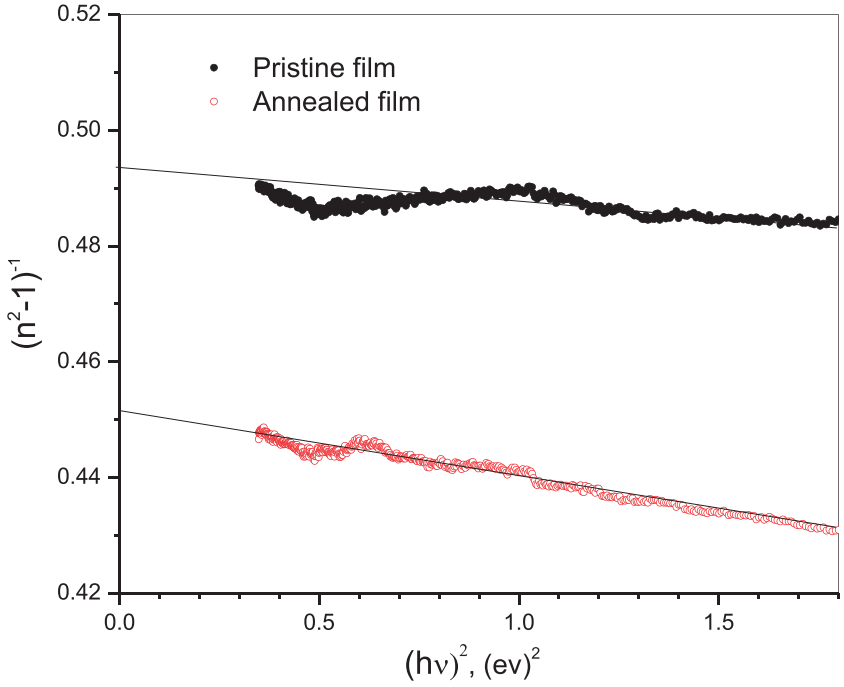

Fig. 8. Plots of $(n^2-1)^{-1}$ versus $(h\nu)^2$ for the pristine and annealed PAHC thin films.

Annealing temperature of PAHC films shifts the absorption edge toward the short wavelength (blue shift), reduces the value of absorbance for wavelength >359 nm and increases it in for wavelength <359 nm. Kasha's exciton model [35] interprets the blue shift as a case of in-line dipoles transition that occur for the long geometrical axes of the molecule to be parallel to polarization axes, but with transition dipoles polarized along the short axis of a unit molecule. The magnitude of the blue shift is consistent with the increase in the optical band gap between the highest occupied molecular orbital (HOMO) and lowest unoccupied molecular orbital (LUMO).

3.2.1. The spectral distribution of transmittance and reflectance of films

Fig. 4 illustrates the spectral behavior of $T(\lambda)$ and $R(\lambda)$ measured at normal incidence of light in the wavelength range 190–2100 nm for pristine and annealed PAHC thin films with a thickness of 170 nm. The transmittance edge divides the spectrum into two transmission regions;. For wavelength <500 nm, the total sum of $R(\lambda)$ and $T(\lambda)$ is less than unity. Therefore the PAHC films are considered to be good absorbers for light. At long wavelength >500 nm, $T(\lambda)$ is greater than $R(\lambda)$ and their total sum approaches unity. The material is transparent for light and the value of absorption index approaches from zero. Therefore, in that transparent region we can calculate the value of refractive index and dispersion parameters for these films. Annealing PAHC films at 423 K increases the transmittance and reflectance spectra and shifts the transmittance edge to the low wavelength side (blue shift) which indicates an increase in the value of the optical energy gap.

The optical properties of different materials can be characterized by the complex refractive index, n^*, where $n^* = n + ik$. In general, the real part, n, is related to the dispersion, while the imaginary part, k, provides a measure of dissipation rate of the electromagnetic wave in the dielectric medium. The values of refractive and absorption indices for PAHC thin films are computed using the absolute values of transmittance and reflectance. The refractive index, n, and the absorption index, k, of thin films deposited onto thick non-absorbing substrates can be calculated by using the following equations, respectively [36,37]:

$$n = \left(\frac{4R}{(1-R)^2} - k^2\right)^{1/2} + \left(\frac{1+R}{1-R}\right) \quad (6)$$

$$k = \frac{\alpha\lambda}{4\pi} \quad (7)$$

$$\alpha = \left(\frac{1}{d}\right)\ln\left[\left(\frac{(1-R)^2}{2T}\right) + \left(\left(\frac{(1-R)^4}{4T^2}\right) + R^2\right)^{1/2}\right] \quad (8)$$

where α and d are the absorption coefficient and the film thickness, respectively. The spectral distribution of the refractive index, n, and absorption index, k, for PAHC thin films in the pristine and annealed conditions is illustrated in Fig. 5. It shows an anomalous dispersion in the range from 200 to 860 nm with one dispersion peak for PAHC; however, a multi-oscillator model can explain the anomalous dispersion region. Annealing temperature increases the value of the refractive and extinction indices all over the spectra for PAHC thin film. The results of refractive index, n, depicted in Fig. 5 shows dispersion peaks in UV–vis region of spectra; these are attributed to electronic transition across π–π^* and $n \rightarrow \pi^*$ orbital. The increases in the value of the refractive and extinction indices, with annealing temperatures is due to enhanced aggregation of PAHC molecules by annealing where most of monomers of PAHC is transformed to oligomers and the film structure becomes more ordered [38].

3.2.2. Absorption coefficient and optical energy band gap

The spectral distribution of the absorption coefficient, α, was calculated for the studied films in the wavelength range 200–2200 nm using the corresponding values of $T(\lambda)$ and $R(\lambda)$ as in relation (6). A typical absorption coefficient spectra of PAHC films in the pristine and annealed conditions are shown in Fig. 6. PAHC

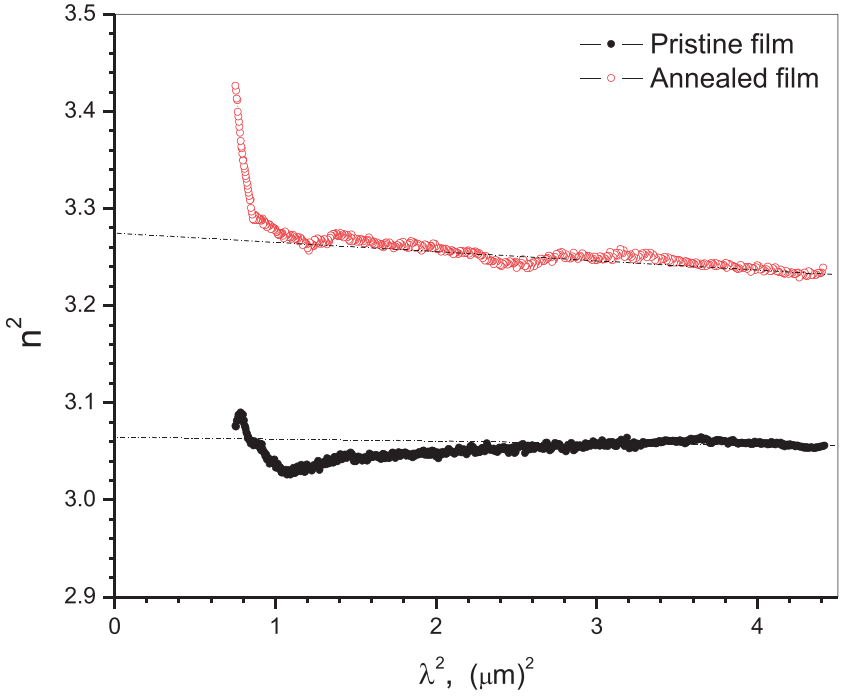

Fig. 9. Relation between, n^2, and, λ^2, for the pristine and annealed PAHC thin films.

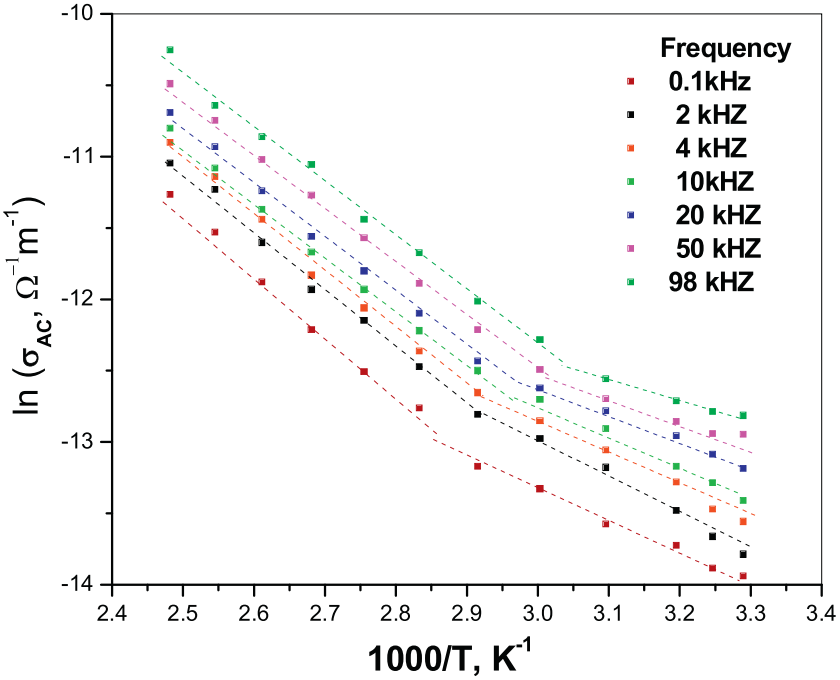

Fig. 10. Logarithmic of AC conductivity for Au/PAHC/Au in sandwich configuration as a function of reciprocal temperature for different frequencies.

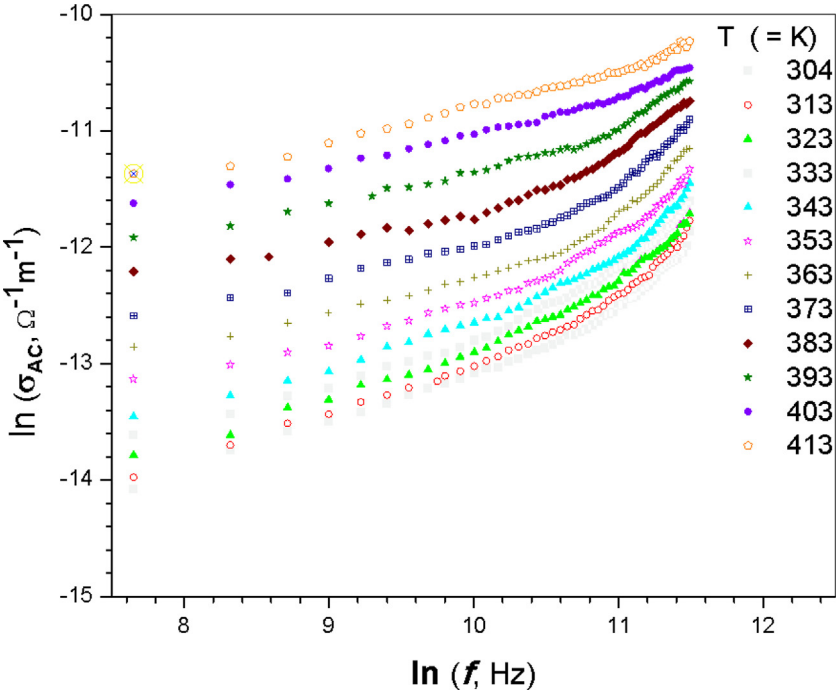

Fig. 11. The frequency dependence on AC conductivity, σ_{AC}, at various temperatures for PAHC films.

films have high absorption coefficient value. The absorption coefficient spectrum reveals three bands with peaks at 2.77, 4.5 and 5.5 eV in the visible and UV regions of spectra, respectively. These absorption bands are attributed to electronic transitions across the $\pi \rightarrow \pi^*$ and $n \rightarrow \pi^*$ orbitals over the UV and visible regions. The position of peaks and absorption edge shift to high photon energy with increasing the annealing temperature.

The type of the electron transition and the value of the optical energy band gap, E_g, may be determined from the analysis of the absorption coefficient, α, near to the onset and the optical absorption edges. The relation between absorption coefficient, α, and photon energy is introduced by Tauc's equation [39]. This equation is used to investigate optically induced electronic transitions in terms of band-to-band transition and optical band-gap energy for amorphous semiconductor and can be expressed as:

$$\alpha h\upsilon = C(h\upsilon - E_g)^r \quad (10)$$

where C is a constant depending on transition probability, $r = 2$ or 3 for indirect allowed and forbidden transitions, respectively and $r = 1/2$ or $3/2$ for direct allowed and forbidden transitions, respectively. The dependence of $(\alpha h\upsilon)^{1/r}$ on photon energy $(h\upsilon)$ for onset and fundamental gaps were discussed and plotted for different values of r. The best fit of the experimental results was obtained for $r = 1/2$ as illustrated in Fig. 7. This is the characteristic behavior of direct allowed transition.

The relation between $(\alpha h\upsilon)^2$ and $(h\upsilon)$ for the pristine and annealed films is linear in the region of strong absorption edge for PAHC films. The extrapolation of the straight portion of graphs intercepts the abscissa axis in the values of the optical energy band gap as shown in Fig. 7. The values of optical direct allowed energy gap, E_g^d, for the pristine and annealed films are 2.14 and 2.21 eV, respectively, it is obvious that the energy gap increases with increasing the annealing temperature. Annealing temperature caused partial transformation of amorphous phase of PAHC to nanocrystallite as shown in Fig. 1(b), this result in a reduction of the structural disorder and a removal of trap levels near from LUMO and HOMO bands. This in turn decreases the number of localized states in the band gap. As a direct consequence, the absorption index increases and the absorption edge shifts to high energies resulting in an increase in the energy gap [40]. The increasing of energy band-gap upon annealing temperature has been observed in some literature about different organic compounds thin films [40,41].

3.3. Dispersion characteristics

In the transparent region of spectra, the spectral dependence of refractive index can be explained by adopting single oscillator model proposed by Wemple and DiDomenico [42,43], in this model the refractive index is related to the dispersion parameters by:

$$\frac{1}{n^2-1} = \frac{E_o}{E_d} - \frac{1}{E_o E_d}(h\upsilon)^2 \tag{11}$$

where $h\upsilon$ is the photon energy, E_o is the oscillator energy that gives quantitative information on the overall band structure of the material and E_d is the dispersion energy which is a measure of the strength of inter-band optical transition inside the material. A plot of $(n^2-1)^{-1}$ versus $(h\upsilon)^2$ for PAHC film in the pristine and annealed conditions are illustrated in Fig. 8. The oscillator energy, E_o, and the dispersion energy, E_d, are directly determined from the slope $(E_o/E_d)^{-1}$ of the linear portion of the curve and its intercept with ordinate axis (E_o/E_d). The intercept of the linear portion of the curve with ordinate axis determines also the value of ε_∞ ($\varepsilon_\infty = n^2$ at $(h\upsilon) = 0$). The values of E_o and E_d for the pristine and annealed films are listed in Table 3. It is noticed that E_o and E_d decrease by annealing temperatures. It is clear that the values of E_g and E_o satisfy the relationship $(E_o \approx 2E_g)$, which had been suggested by Tanaka [44].

The lattice dielectric constant, ε_L, and the ratio of carrier concentration to the effective mass, N/m^*, in the transmission region of spectra can be also deduced from the relation [43,45]:

$$n^2 = \varepsilon_L - \left(\frac{e^2}{4\pi^2\varepsilon_o c^2}\right)\left(\frac{N}{m^*}\right)\lambda^2 \tag{12}$$

where N/m^* is the ratio of the carrier concentration to the electron effective mass, e is the electron charge and c is the velocity of the light. The graphical representation of n^2 as a function of λ^2 for the pristine and annealed PAHC film is shown in Fig. 9. By extrapolating the linear part toward the shorter wavelength, the intercept with the ordinate axis (at $\lambda = 0$) gives the value of ε_L and from the slopes of these lines the ratio N/m^* can be calculated. It is clear that $\varepsilon_L \approx \varepsilon_\infty$ and this confirms the theory. The results of the influence of annealing temperature on dispersion parameters of PAHC films are listed in Table 3. Annealing temperature decreases the values of dispersion parameters in comparison to those values of the pristine PAHC film.

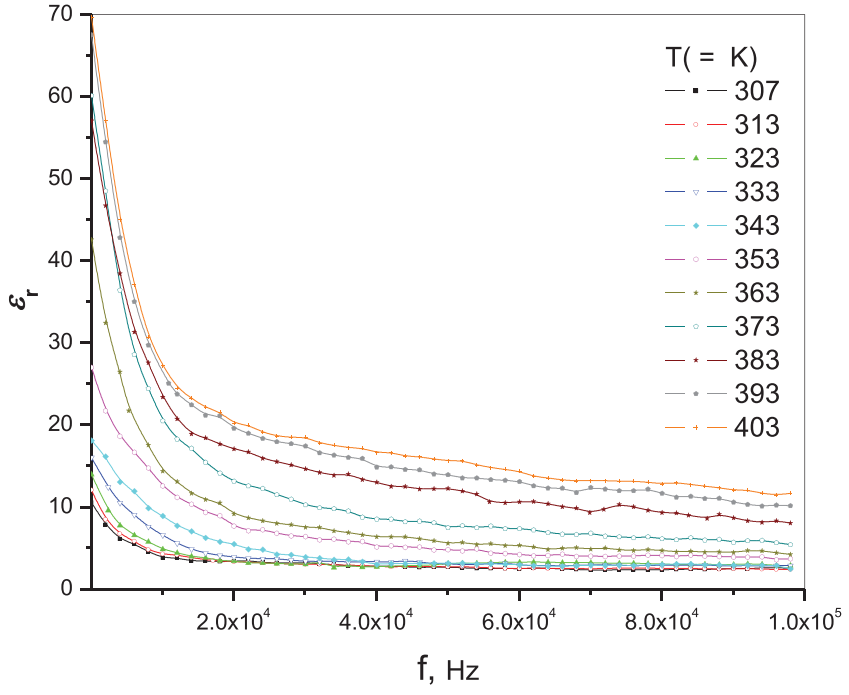

Fig. 12. Frequency dependence of the real part of the dielectric constant, ε_r, for PAHC thin films at different temperatures.

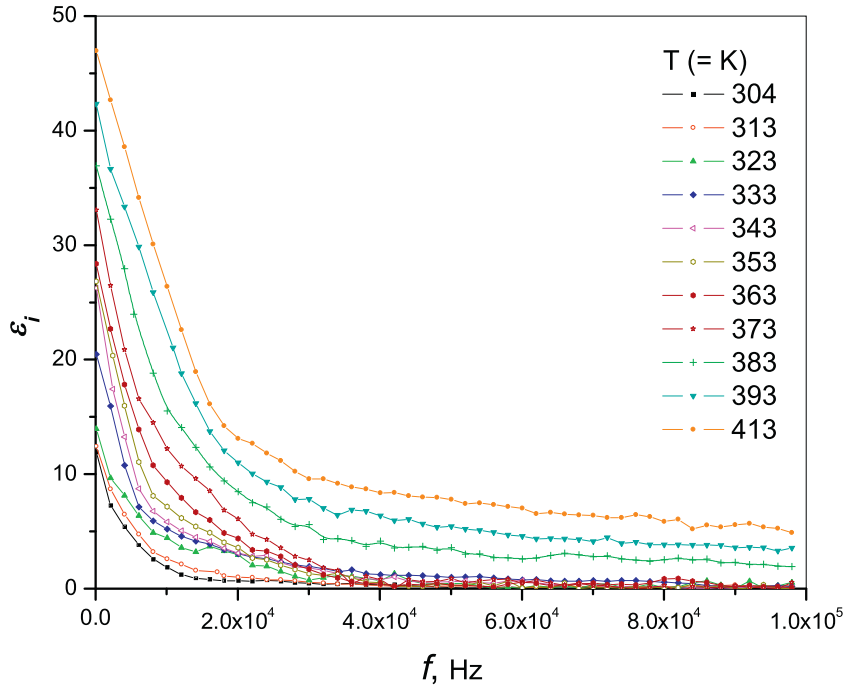

Fig. 13. Frequency dependence of imaginary part of dielectric constant, ε_i, for PAHC thin films at different temperatures.

3.4. AC conductivity and dielectric constants of PAHC thin films

AC electrical conductivity measurements of semiconductors have been extensively used to understand the electronic transport mechanisms and are a powerful tool for obtaining information about the defect states in amorphous semiconductors. The temperature dependence of AC conductivity suggests that it is a thermally-activated process and it can be interpreted according to Arrhenius equation [46,47]:

$$\sigma_{AC} = \sigma_0 \exp\left(\frac{-\Delta E}{k_B T}\right) \tag{13}$$

where σ_o is the pre-exponential factors, E_a is the activation energy for this thermally activated process, T is the temperature expressed in Kelvin and k_B is the Boltzmann constant. The plot of $\ln \sigma_{AC}$ versus reciprocal temperature ($1000/T$) in the temperature range 304–413 K is shown in Fig. 10. It is clear that $\ln \sigma_{AC}$ increases linearly with the reciprocal temperature and shows two linear regions with different slopes (regions I and II). The total conductivity σ_{total} of many semiconductors [48] over a wide range of frequencies, ω, and temperature, T, can be written as:

$$\sigma_{total} = \sigma_{AC} + \sigma_{DC} \tag{14}$$

where σ_{AC} is the AC conductivity and σ_{DC} is the DC conductivity. This equation is valid only when the AC and DC conductions arise from completely separate mechanisms, but when $\omega \to 0$, the DC conductivity represents the total conductivity

Eq. (14) can be rewritten according to Arrhenius Eq. (13) as follow:

$$\sigma_{ac} = \sigma_I \exp\left(\frac{-\Delta E_I}{k_B T}\right) + \sigma_{II} \exp\left(\frac{-\Delta E_{II}}{k_B T}\right) \tag{15}$$

where ΔE_I and ΔE_{II} are the thermal activation energies at low and high temperatures, respectively; and σ_I and σ_{II} are the pre-exponential factors at low and high temperatures, respectively. The thermal activation energies, ΔE_I and ΔE_{II}, for PAHC films are calculated from the slope of the straight line of the two segment in the $\ln \sigma_{AC} - 1000/T$ curves. At high temperature region, the magnitude of ΔE_{II} varies from 0.92 to 0.98 eV which is nearly half the value of the optical band-gap that obtained from optical measurements (2.12 eV). This indicates that the conduction in this region is due to intrinsic process [48]. Referring to the activation energy estimated at lower temperatures (ΔE_I) are in the range (0.24–0.28) eV, the conduction in this region can be ascribed to the extrinsic process [49], in which the activation energy is needed to excite the carriers from the corresponding trap levels to the conduction band.

Fig. 11 shows the relation between $\ln \sigma_{AC}$ and $\ln f$ for Au/PAHC/Au sandwich film in the temperature range 304–413 K. The logarithm of AC conductivity increases linearly with logarithm of frequency. The AC conductivity mentioned in Eq. (12) can be expressed in another form as a function of frequency [50,51]:

$$\sigma_{AC}(\omega) = A\omega^S \tag{16}$$

where S is the frequency exponent and A is a constant depending on the temperature. S is a characteristic parameter associated with charge carriers or extrinsic dipoles arising from the presence of defects or impurities. The values of S at different temperatures were calculated from the slope of the linear part of the relation $\ln \sigma_{AC} - \ln f$. S values decreases from 0.67 to 0.39 as the temperature increases from 303 to 413 K, respectively. This indicates that correlated barrier hopping is the dominant conduction mechanism [48].

The dielectric relaxation studies are important to understand the nature and the origin of dielectric losses, which may be useful in the determination of the structure and defects in solids. The complex dielectric can be expressed as [50,51]:

$$\varepsilon^*(\omega) = \varepsilon_r(\omega) + i\varepsilon_i(\omega) \tag{17}$$

where ε_r and ε_i are the real and imaginary parts of the dielectric constant, respectively. The value of ε_r can be calculated using the formula:

$$\varepsilon_r = \frac{C_p d}{\varepsilon_o A} \tag{18}$$

Where C_p is the parallel capacitance, d is the thickness of the film, ε_o is the permittivity of free space and A is the active area of the sample. ε_i can be calculated using the formula:

$$\varepsilon_i = \varepsilon_r \tan\delta \quad (19)$$

where $\tan\delta$ is the loss tangent, which is a part of the energy of an electric field dissipated as heat in dielectric medium and it is comprised of two parts: the first one arises from the electrodes resistance and is influenced at high frequencies. This can be minimized using the electrodes of high conducting metal (Ohmic electrodes). The second part is a property of the dielectric material itself and it is frequency dependent.

Figs. 12 and 13 illustrate the variation of ε_r and ε_i with frequency at different temperatures. It is clear from these figures that $\varepsilon_r > \varepsilon_i$ and they have the same behavior with frequency and temperature; where they decrease with increasing frequency and they increase with temperature. Also it can be observed that the ε_r and ε_i exhibit strong temperature dependence at high temperatures and low frequencies. The behavior of ε_r and ε_i with frequency can be explained as follows; at low frequencies the dielectric constant ε_r, and dielectric loss, ε_i, for polar material is due to the contribution of polarizability, deformational polarization (electronic and ionic polarization) and relaxation polarization (orientation and interfacial polarization) [52]. As the frequency is increased, the dipoles will no longer be able to rotate sufficiently rapidly, so that their oscillations begin to lag behind those of the field. As the frequency is further increased, the dipole will be completely unable to follow the field and the orientation polarization stopped, so ε_r and ε_i decreases at higher frequencies approaching a constant value due to the interfacial or space charge polarization only [53].

4. Conclusions

3-phenyl azo-4-hydroxycoumarin, PAHC, thin films have been grown successfully on the glass and quartz substrates by using thermal evaporation technique under high vacuum. The structure characterizations have been analyzed by XRD and FTIR techniques. XRD of PAHC compound shows polycrystalline phase in powder form; it becomes nanocrystallite dispersed in amorphous phase upon thermal deposition to form a thin film. Annealing temperatures increase the crystallite size, decreases dislocation density and improve crystallinity of these films. FTIR spectra of the powder, pristine and annealed films revealed that the chemical composition of PAHC has been preserved by thermal evaporation technique. The optical constants of PAHC thin films were investigated before and after annealing in the spectral range 200–2100 nm using spectrophotometric measurements. The optical constants were calculated from measurements of transmittance and reflectance of PAHC films. The single oscillator model has been used to analysis the dispersion parameters before and after annealing process. The refractive index n and absorption index k increases with increasing annealing temperature. Lattice dielectric constant ε_L, is approximately equal to the high-frequency dielectric constant, ε_∞; this confirms the theory and they increase by annealing. The oscillator energy, E_o, the dispersion energy, E_d, and N/m^* of the PAHC thin films decrease with increasing annealing temperature. Direct allowed transition is observed in PAHC films and the optical energy gap of PAHC film is 2.14 and 2.21 eV for pristine and annealed films, respectively. The annealing temperature has an obvious effect on the optical properties of PAHC thin films. The alternating current conductivity, σ_{ac}, and dielectric properties of PAHC thin films are investigated in investigated in temperature range 304–413 K and frequency range 0.1–100 kHz. The real and imaginary parts of the dielectric constants, ε_i and ε_r, increase with increasing the temperature and they decrease with increasing frequency. Future work may be focused on using the proposed PAHC material in the synthesis of photovoltaic devices.

References

[1] A. Boucherif, G. Beaudin, V. Aimez, R. Arès, Appl. Phys. Lett. 102 (1) (2013) 0119151–0119155.
[2] K. Xue, G. Han, B. Chen, P. Chen Y. Duan, Org. Electron. 26 (2015) 225–229.
[3] Yu-Fu Wang, M.R. Tsai, Yi-S. Lin, Fu-C. Wu, C.Y. Lin, H.L. Cheng, S.J. Liu, Fu-C. Tang, W.-Y. Chou, Org. Electron. 26 (2015) 359–364.
[4] M.M. Makhlouf, H.M. Zeyada, Solid State Electron. 105 (2015) 51–57.
[5] Li Fan, S.Q. Gao, Z. Bo Li, W.F. Niu, W.J. Zhang, S.M. Shuang, C. Dong, Sens. Actuators B: Chem. 221 (2015) 1069–1076.
[6] D. Audisio, S. Messaoudi, I. Ijjaali, E. Dubus, F. Petitet, J.F. Peyrat, J.D. Brion, M. Alami, Eur. J. Med. Chem. 45 (2010) 2000–2009.
[7] S. Yadav, S.K. Singh, S.K. Mangawa, U. Dixit, Y. Gupta, S.K. Khajuria, Spectrochim. Acta A 148 (2015) 311–317.
[8] H. Li, L. Cai, J. Li, Y. Hu, P. Zhou, Dyes Pigments 91 (2011) 309–316.
[9] M. Richard, P.Y. Massonneau, A. Renard, Org. Lett. 10 (2008) 4175–4178.
[10] Y. Chen, K.-H. Chen, J. Polym. Sci. A: Polym. Chem. 35 (1997) 613–624.
[11] N.K. Mal, M. Fujiwara, Y. Tanaka, T. Taguchi, M. Matsukata, Chem. Mater. 15 (2003) 3385–3394.
[12] H.C. Kim, S. Hartner, M. Behe, T.M. Behr, N. Hampp, J. Biomed. Opt. 11 (2006) 034024-1.
[13] A. Nagata, T. Sakaguchi, T. Ichihashi, M. Miya, K. Ohta, Macromol. Rapid Commun. 18 (1997) 191–196.
[14] F.J. Duarte, L.W. Hillman (Eds.), Dye Lasers, Springer, New York, 1990 p. 390.
[15] P. Hauser, Textile Dyeing, InTech, Rijeka, Croatia, 2011, pp. 195–220.
[16] L. Du, M. Li, S. Zheng, B. Wang, Tetrahedron Lett. 49 (2008) 3045–3048.
[17] P.S. Song, W.H. Gordon, J. Phys. Chem. 74 (1970) 4234–4240.
[18] J.S. de Melo, P.F. Fernandes, J. Mol. Struct. 565 (2001) 69–78.
[19] A.O. Obaseki, W.R. Porter, W.F. Trager, J. Heterocycl. Chem. 19 (2) (1984) 385–390.
[20] Y.K. Al-Majedy, A.A.H. Kadhum, A.A. Al-Amiery, A.B. Mohamad, Molecules 19 (2014) 11791–11799.
[21] J. Gaultier, C. Hauw, Acta Crystallogr. 20 (1966) 646–651.
[22] M.M. Hussain, R. Sindhu, H.C. Tandon, Eur. J. Chem. 3 (1) (2012) 75–80.
[23] R. Giri, S.S. Rathi, M.K. Machwe, Spectrochim. Acta A 44 (1988) 805–807.
[24] S. Kumar, V.C. Rao, R.C. Rastogi, Spectrochim. Acta A 57 (2001) 41–47.
[25] S.A. Azim, S.M. Al-Hazmy, E.M. Ebeid, S.A. El-Daly, Opt. Laser Technol. 37 (2005) 245–249.
[26] J. Basavaraja, S.R. Inamdar, H.M.S. Kumar, Spectrochim. Acta A 137 (2015) 527–534.
[27] R. Shirley, The CRYSFIRE System for Automatic Powder Indexing: User's Manual, The Lattice Press, Guildford, Surrey GU2 7NL, England, 2000.
[28] J. Laugier, B. Bochu, LMGP-Suite of Programs for the Interpretation of X-ray Experiments, ENSP/Laboratoire des Materiaux et du Genie Physique, BP 46. 38042, Saint Martin d'Heres, France, 2000.
[29] V. Manjunatha, K. Subramanya, H. Devendrappa, Compos. Interfaces 21 (2) (2014) 121–131.
[30] E.R. Shaaban, M.A. Kaid, M.G.S. Ali, J. Alloy Compd. 613 (2014) 324–329.
[31] R.M. Saumya, K.T. Awalendra, R.N.P. Choudhary, Ionics 14 (2008) 255–262.
[32] F. Cavani, F. Trifiróand, A. Vaccari, Catal. Today 11 (2) (1991) 173–301.
[33] R. Giustetto, K. Seenivasan, D. Pellerej, G. Ricchiardi, S. Bordiga, Microporous Mesoporous Mater. 155 (2012) 167–176.
[34] W.R. Scheidt, Stereochemistry of porphyrin derivatives, in: D. Dolphin (Ed.), Review Article, The Porphyrins. III, Academic Press, 1978, pp. 463–511.
[35] M. Kasha, H.H. Rawls, A. El-Bayoumi, Pure Appl. Chem. 11 (34) (1965) 371–392.
[36] M. Fox, Optical Properties of Solids, Oxford University Press, 2007.
[37] H.M. Zeyada, M.M. Makhlouf, M.I.M. Ismail, A.A. Salama, Mater. Chem. Phys. 163 (2015) 45–53.
[38] Z. Gu, J. Yin, P. Liang, F. Gan, Opt. Mater. 27 (2005) 1618.
[39] J. Tauc, Amorphous and Liquid Semiconductors, Plenum Press, New York, 1974.
[40] H.M. Zeyada, M.M. EL-Nahass, I.S. Elashmawi, A.A. Habashi, J. Non Cryst. Solids 358 (3) (2012) 625–636.
[41] M.H. Habibi, N. Talebian, Acta Chim. Slov. 52 (2005) 53–59.
[42] S.H. Wemple, M. DiDomenico, Phys. Rev. Lett. 23 (1969) 1156–1160.
[43] M.M. Makhlouf, A. El-Denglawey, H.M. Zeyada, M.M. El-Nahass, J. Lumin. 147 (2014) 202–208.
[44] K. Tanaka, Thin Solid Films 66 (1980) 271–279.
[45] H.M. Zeyada, M.M. Makhlouf, M.M. El-Nahass, Spectrochim. Acta A 148 (2015) 338–347.
[46] N.F. Mott, Electronic Processes in Non-crystalline Materials, Clarendon, 1971.
[47] H.M. Zeyada, M.M. El-Nahass, M.M. Makhlouf, Curr. Appl. Phys. 11 (2011) 1326–1331.
[48] S.R. Elliott, Philos. Mag. B 37 (1978) 553–560.
[49] M.M. El-Nahass, K.F. Abd-El-Rahman, A.A.A. Darwish, Phys. B 403 (2008) 219–232.
[50] A.K. Jonscher, Nature 267 (1977) 673–679.
[51] H. Zeyada, M.M. Makhlouf, Appl. Phys. A 119 (2015) 1109–1118.
[52] R. Ertuğrul, A. Tataroğlu, Chin. Phys. Lett. 29 (7) (2012) 077304–077305.
[53] M.M. El-Nahass, A.A. Atta, E.F.M. El-Zaidia, A.A.M. Farag, A.H. Ammar, Mater. Chem. Phys. 143 (2) (2014) 490–494.